Analytical, Numerical, and Experimental Analysis of Inverse Macrosegregation during Upward Unidirectional Solidification of Al-Cu Alloys

IVALDO L. FERREIRA, CARLOS A. SANTOS, VAUGHAN R. VOLLER, and AMAURI GARCIA

The present work focuses on the influence of alloy solute content, melt superheat, and metal/mold heat transfer on inverse segregation during upward solidification of Al-Cu alloys. The experimental segregation profiles of Al 4.5 wt pct Cu, 6.2 wt pct Cu, and 8.1 wt pct Cu alloys are compared with theoretical predictions furnished by analytical and numerical models, with transient h_i profiles being determined in each experiment. The analytical model is based on an analytical heat-transfer model coupled with the classical local solute redistribution equation proposed by Flemings and Nereo. The numerical model is that proposed by Voller, with some changes introduced to take into account different thermophysical properties for the liquid and solid phases, time variable metal/mold interface heat-transfer coefficient, and a variable space grid to assure the accuracy of results without raising the number of nodes. It was observed that the numerical predictions generally conform with the experimental segregation measurements and that the predicted analytical segregation, despite its simplicity, also compares favorably with the experimental scatter except for high melt superheat.

I. INTRODUCTION

DURING solidification of alloys, segregation results from the various ways in which the solute elements and impurities can become redistributed within the solidified structure. Based on the scale of the segregation phenomena, it may be divided into two parts: microsegregation and macrosegregation. Microsegregation includes short-range differences in chemical composition, such as those found between cells, dendrites, and grains. When the compositional difference shows long-range variation, for instance, between the outside and inside of a casting or ingot, this is considered macrosegregation. These phenomena may result in varying the chemical composition on the microscopic and macroscopic levels within a casting. This compositional heterogeneity of the cast structure induces nonuniformity of mechanical properties.

In conditions of pronounced dendritic growth, the interdendritic channels contain liquid of a high solute content because of lateral diffusion of solute. For most metals, there is a contraction on solidification and the high solute liquid is drawn toward the actual freezing interface at the base of the dendrite stalks, producing abnormally high solute concentrations at the outer regions of the ingot. This condition is known as inverse segregation because the solute distribution is opposite to that expected for normal segregation where the center of the ingot may be of higher solute concentration than the outside. Inverse segregation has been reported to be caused mainly by solidification contraction and favored by slow cooling rate, wide freezing range of the alloy, and coarse dendrite arm spacings.[1,2] In the region adjacent to the outside face, the inverse segregation profile drops rapidly with distance from the chill face, and was found to decrease with increasing melt superheat and to decrease as the thermal conductivity of the chill material decreased.[3]

Another important type of segregation can result when the semisolid external surface of the casting begins to contract from the mold wall, leaving a space into the interdendritic liquid can flow. The flow is driven by the pressure drop due to the air gap formation. A thin layer of highly segregated material, referred to as exudation, is then formed at the surface of the casting. While inverse segregation is positive from the casting surface, a negative segregation profile will be formed along the semisolid shell through which exudation has taken place, since it is depleted of alloying elements.[4,5]

Scheil[6] was the first to treat inverse segregation with an analytical expression that can predict the maximum segregation at the chill face as a function of alloy composition. Kirkaldy and Youdelis[7] extended Scheil's equation to predict not only the maximum segregation, but also the positional variation of the segregation in a unidirectionally solidified ingot. Several studies in the literature have reported that the Kirkaldy–Youdelis's approach accounts for the inverse solidification profile along the ingot length.[8–11]

Flemings et al.[12,13,14] proposed a model, which assumes the interdendritic liquid driven only by contraction on solidification; the solute was neglected and the temperature gradients and velocity distributions were measured or assumed. The derived "local solute redistribution equation" was shown to predict successfully the formation of macrosegregation, particularly inverse segregation for unidirectional solidification of Al-Cu alloys.

Tsai and co-workers[15,16] have employed the continuum formulation, including the fluid flow and domain change caused by solidification contraction, to develop a model that was applied to investigate the inverse segregation during unidirectional solidification of Al-Cu alloys cooled from the bottom. Chang and Stefanescu[17] have also developed a model

IVALDO L. FERREIRA, Doctoral Student, CARLOS A. SANTOS, Postdoctoral Fellow, and AMAURI GARCIA, Professor, are with the Department of Materials Engineering, State University of Campinas, UNICAMP, 13083-970, Campinas, SP, Brazil. VAUGHAN R. VOLLER, Professor, is with the Department of Civil Engineering, University of Minnesota, Minneapolis, MN 55455-116. Contact e-mail:amaurig@fem.unicamp.br
Manuscript submitted April 9, 2003.

based on the continuum formulation, assuming that the inter-dendritic liquid flow was driven by thermal and solutal buoy-ancy as well as by solidification contraction. Validation of the model was performed for the case of inverse segregation in a directionally solidified Al 4.0 wt pct Cu casting with equiaxed grains.

In a recent article, Voller[18] proposed a numerical approach for the coupling of species and thermal transport. In the context of a model of the inverse segregation occurring in a binary alloy (but it deals with multicomponent alloy), he demonstrated that his approach could easily handle the key features in the coupling thermal and solutal fields, e.g., eutectic reactions, and also is accurate, i.e., the proposed numerical scheme and his associated code accurately solved the governing partial differential equations that make up the model. Voller[19] compared the basic mechanics in the thermal and solutal fields numerically and analytically making use of a sophisticated similarity solution of inverse segregation. One important characteristic of this numerical approach is the use of an explicit/implicit time integration scheme that leads to a significant saving in computer time and also allows for a straightforward treatment of key phenomena such as eutectic reactions. In essence, the coupling involves taking a nodal value (macroscopic point value) and invoking a micromodel (which is a constitutive equation) to arrive at thermal and solutal fields, which are consistent with the thermodynamics of the problem. In a more recent article,[20] the analytical solution proposed by Voller has been extended to encompass flow in the bulk liquid, mushy properties, and microsegregation parameters such as partition coefficients, which are different for all solute species.

The present work focuses on the influence of alloy solute content, melt superheat, and transient metal/mold heat-transfer coefficients (h_i) on the positional variation of inverse segregation during upward solidification of Al-Cu alloys. The experimental segregation profiles of Al 4.5 wt pct Cu, 6.2 wt pct Cu, and 8.1 wt pct Cu alloys are compared with theoretical predictions furnished by analytical and numerical models, with transient h_i profiles being determined in each experiment by an automatic search of the best fitting among theoretical and cooling curves in metal. The analytical model is based on an analytical heat-transfer model coupled with the classical local solute redistribution equation. The numerical model is that proposed by Voller,[18] with some changes introduced to take into account different thermophysical properties for the liquid and solid phases, time variable metal/mold interface heat-transfer coefficient, and variable space grid to assure the accuracy of results without raising the number of nodes.

II. ANALYTICAL MODEL

A. Inverse Macrosegregation

Flemings and Nereo[14] proposed a model to predict various types of segregation, such as inverse macrosegregation. This model is based on mass balance considering a small volume element (x,y,z) within ingot during solidification. Their considerations were as follows: the element is large enough that the fraction solid within it at any time is exactly the local average, but small enough that it can be treated as a differential element; no solid material enters or leaves the volume element during solidification; solute enters or leaves the element only by liquid flow to feed shrinkage; and liquid composition and temperature within the element are uniform (within a differential amount) at any time. Conservation of solute mass in the volume element along solidification requires that

$$\frac{\partial}{\partial t}(\bar{\rho}\bar{C}) = -\nabla \cdot \rho_L\, g_L C_L V_F \qquad [1]$$

where t is time (seconds), $\bar{\rho}$ is the local average density (solid + liquid) (kg/m^3), $\bar{C}$ is the local average composition (solid + liquid) (wt pct), ρ_L is the liquid density, g_L is the volume fraction of liquid, C_L is the liquid composition within the volume element, and V_F is the local velocity of interdendritic liquid relative to solid (m/s). Equation [1] is used to derive the well-known "local solute redistribution equation," which is used to calculate macrosegregation, and is given by

$$\frac{\partial g_L}{\partial C_L} = -\left(\frac{1-\beta}{1-k_0}\right)\left(1 + \frac{V_F \cdot G}{\overset{0}{T}}\right) \cdot \frac{g_L}{C_L} \qquad [2]$$

where $\beta = (\rho_S - \rho_L)/\rho_S$ is the solidification shrinkage, k_0 is the partition coefficient, G is the thermal gradient (K/m), and $\overset{0}{T}$ is the cooling rate (K/s). Equation [2] is written for uni-directional heat flow conditions, i.e., with planar isotherms moving perpendicular to a determined axis assuming constant solid density during solidification, negligible net solute change from diffusion, and no pore formation.

Equation [2] can be used to predict the formation of inverse macrosegregation if V_F, G, and $\dot{T}$ are measured experimentally or calculated from heat flow considerations.

B. Analytical Solidification Model

An analytical heat-transfer model, which describes the temperature distribution and the position of solidus and liquidus isotherms in the unidirectional solidification of binary alloys, can be coupled with the Flemings and Nereo's solution, providing the solidification thermal parameters necessary in the determination of the inverse macrosegregation profile in the solid. The model is an extension of the one developed earlier by Garcia and Prates for pure metals cooled by fluids, for pure metals solidifying against a massive uncooled mold, or for alloys solidifying against a cooled or massive mold.[21,22] The model employs the mathematically expedient technique of replacing the interfacial resistance by equivalent layers of material, and the latent heat of fusion is taken into account by adjusting the specific heat over the solidification temperature range. The ingot is treated as a one-dimensional moving boundary problem with boundaries at the tips and roots of the dendrites. It is assumed that the Newtonian interface resistance is represented by a transient metal/mold heat-transfer coefficient (h_i). The other thermophysical properties describing the system are treated as averages within the same phase, as follows:

$$\text{Metal}\begin{cases} T > T_{\text{Liq}} & k_L, \rho_L, c_L & [3] \\[4pt] T_{\text{Sol}} < T < T_{\text{Liq}} & \begin{cases} k_{SL} = (k_S + k_L)/2 & [4] \\ \rho_{SL} = (\rho_S + \rho_L)/2 & [5] \\ c_{SL} = c_L + [\Delta H/ \\ \quad (T_{\text{Liq}} - T_{\text{Sol}})] & [6] \end{cases} \\[4pt] T < T_{\text{Sol}} & k_S, \rho_S, c_S & [7] \end{cases}$$

where T_{Liq} is the liquidus temperature (Kelvin), T_{Sol} is the nonequilibrium solidus temperature, k is the thermal conductivity (W/m · K), c is the specific heat (J/kg · K), ΔH is the latent heat of fusion (J/kg), and h_i(W/m^2 · K).

The one-dimensional Fourier field equation is exactly applicable to the virtual metal/mold system, and the solution obtained in the system can be related to the real system by simple relationships. The model has been detailed in previous articles and validated against experimental data describing the unidirectional solidification of Al-Cu, Zn-Al, and Sn-Pb alloys.[23,24,25] The temperature gradient (G_L) and the growth rates at the dendrite tips (V_L) and roots (V_S) are given, respectively, by

$$V_S = \frac{2\alpha_S\phi_1^2}{\left[\dfrac{2k_S\phi_2\,(T_{Sol} - T_0)}{n\sqrt{\pi}\,(T_{Liq} - T_0)\,\exp(\phi_1^2)\,[M + \mathrm{erf}(\phi_1)]\,h_i}\right] + S_s} \quad [8]$$

$$V_L = \frac{2\alpha_{SL}\phi_2^2}{\left[\dfrac{2k_S\phi_2\,(T_{Sol} - T_0)}{n\sqrt{\pi}\,(T_{Liq} - T_0)\,\exp(\phi_1^2)\,[M + \mathrm{erf}(\phi_1)]\,h_i}\right] + S_L} \quad [9]$$

$$G_L = \left[\frac{m\,(T_{pour} - T_{Liq})}{\sqrt{\pi}\cdot\alpha_{SL}\,\phi_2\,[1 - \mathrm{erf}(m\phi_2)]\exp(m\phi_2)^2}\right]\cdot V_L \quad [10]$$

By multiplying Eqs. [9] and [10], the individual effects of alloy composition, melt superheat ($\Delta T_{pour} = T_{pour} - T_{Liq}$), and metal/mold heat-transfer coefficient (h_i) can be seen inserted into an expression correlating tip cooling rate ($\dot{T}_L$) and solidification parameters, given by

$$\dot{T}_L = \left[\frac{m\Delta T_{pour}}{\sqrt{\pi}\cdot\alpha_{SL}\,\phi_2\,[1 - \mathrm{erf}(m\phi_2)]\exp(m\phi_2)^2}\right] V_L^2 \quad [11]$$

where m is the square root of the ratio of thermal diffusivities of mushy zone and liquid, $(\alpha_{SL}/\alpha_L)^{1/2}$; T_{pour} is the initial melt temperature (Kelvin); T_0 is the environment temperature; α_S and α_L are the solid and liquid thermal diffusivities, respectively $(k/c \cdot \rho)$ (m^2/s); n is the square root of the ratio of thermal diffusivities of solid and mushy zone $(\alpha_S/\alpha_{SL})^{1/2}$; M is the ratio of heat diffusivities of solid and mold material ($M = 0$ for efficiently cooled molds); and S_L and S_S are the positions of liquidus and solidus isotherms from metal/mold interface (m), respectively. Solidification constants ϕ_1 and ϕ_2 are associated with the displacement of solidus and liquidus isotherms, respectively, and can be determined by the simultaneous solution of the following equations:

$$\frac{(T_{Liq} - T_{Sol})}{\mathrm{erf}(\phi_2) - \mathrm{erf}(n\phi_1)} = \frac{k_S\,\exp[(n^2 - 1)\phi_1^2]}{k_{SL}\,n\,[M + \mathrm{erf}(\phi_1)]}\,(T_{Sol} - T_0) \quad [12a]$$

$$\frac{(T_{Liq} - T_{Sol})}{\mathrm{erf}(\phi_2) - \mathrm{erf}(n\phi_1)} = \frac{k_L\,m\,\exp[(1 - m^2)\phi_2^2]}{k_{SL}\,[1 - \mathrm{erf}(m\phi_2)]}\,(T_{pour} - T_{Liq}) \quad [12b]$$

The integration of Eq. [2] for the unidirectional heat flow condition results in

$$C_S^* = k_0 \cdot C_0\,(1 - f_S)^{\left[\frac{(k_0 - 1)}{(1 - \beta)\left(1 - \frac{V_E}{V_L}\right)}\right]} \quad [13]$$

where C_S^* is the solid composition at the liquid/solid interface and f_S is the solid fraction.

For the case of planar isotherms, the back liquid flux velocity (V_{Fz}) can be considered:[2]

$$V_{Fz} = -\frac{\beta}{1 - \beta}\cdot V_S \quad [14]$$

Equation [8] can be inserted into Eq. [14] in order to permit V_{Fz} to be determined as a function of solidification conditions. The insertion of V_{Fz}, G_L, and $\dot{T}_L$ given by Eqs. [14], [10], and [11], respectively, into Eq. [2] permits the inverse segregation profile to be calculated by Eq. [13]. The local averaged solid solute concentration ($\bar{C}_S$) can be obtained by averaging the concentrations of the primary dendritic and eutectic phases, calculated by

$$\bar{C}_S = \frac{\rho_S\displaystyle\int_0^{1 - f_E} C_S^*\,\partial f_s + \rho_{SE}\,f_E\,C_E}{\rho_S\,(1 - f_E) + \rho_{SE}\,f_E} \quad [15]$$

where f_E is the mass fraction of eutectic phase, C_E is the composition of eutectic phase, and ρ_{SE} is the density of solid eutectic. This analytical approach has been subjected to a preliminary validation in a previous article by comparing the theoretical predictions with the experimental inverse segregation profile that resulted from a directionally solidified Al-Cu ingot.[26]

III. NUMERICAL MODELING

The numerical model that will be used to simulate inverse segregation profiles will be based essentially on that proposed previously by Voller.[18] We have first chosen a simple test problem, as Voller did, to guarantee the reproducibility of the numerical approach comparing with his analytical solution and with that by Chung et al.[20] Some modifications have been incorporated into the original numerical approach, like different thermophysical properties for liquid and solid phases, metal/mold interface variable heat-transfer coefficient, and variable space grid to assure the accuracy of results without raising the number of nodes, when comparing with experimental data, since a time variable metal/mold interface heat-transfer coefficient will introduce a nonlinearity condition at the $z = 0$ boundary condition.[27] Considering the previous exposed, the vertically unidirectional solidification of a binary eutectic alloy is our target problem. At time $t < 0$, the alloy is at molten state, at the nominal concentration C_0, and contained in the insulated mold defined by $0 < z < Z_b$, according to Figure 1. Solidification begins by cooling the metal at the chill ($z = 0$) until the temperature drops below the eutectic temperature T_E. At times $t > 0$, three transient regions are formed: solid, solid + liquid (mushy zone), and liquid. During this process, solute is rejected in the mushy zone and subsequently redistributed by
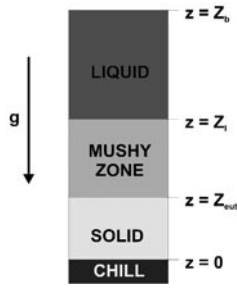
Fig. 1—Schematic inverse segregation problem.

shrinkage-induced fluid flow toward the chill face. It results in a solute-rich layer in the chill region.

In developing the numerical solution for equations of the thermal and solute coupled fields, necessary for the modeling of inverse segregation, the following assumptions were taken.

1. The domain is one-dimensional, defined by $0 < z < Z_b$, where Z_b is a point far removed from the inverse segregation region.
2. The inverse segregation region remains free of porosity.[28]
3. The solid phase is stationary, *i.e.,* once formed has zero velocity.
4. Due to the relatively rapid nature of heat and liquid mass diffusion, in a representative elemental averaging volume,[29] the liquid concentration C_L, the temperature T, the liquid density ρ_L, and the liquid velocity u_L are assumed to be constant.
5. In the phase diagram, the partition coefficient k_o and the liquid slope m_L are assumed to be constants.
6. Equilibrium conditions exist at the solid/liquid interface; *i.e.,* at this interface, we have

$$T = T_F - m_L C_L \qquad [16]$$

and

$$C_S^* = k_0 C_L \qquad [17]$$

where T_F is the fusion temperature of the pure solvent (Kelvin) and C_S^* is the interface solid concentration.

7. The specific heats, c_S and c_L, thermal conductivities, k_S and k_L, and densities ρ_S and ρ_L, are constants within each phase, but discontinuous between the solid and the liquid. The latent heat of fusion is taken as the difference between phase enthalpies $\Delta H = H_L - H_S$.
8. The metal/mold thermal resistance varies with time and is incorporated in a global heat-transfer coefficient defined as h_i.[30]

Thermo-Calc* software[31] can be used to generate equi-

---

*Thermo-Calc software is an exclusive copyright property of the STT Foundation (Foundation of Computational Thermodynamics, Stockholm, Sweden).

---

librium diagrams, and through the Thermo-Calc interface with FORTRAN/C,** it is possible to recall those data gen-

---

**FORTRAN/C is trademark of Microsoft Corporation, Redmond, CA.

---

erated by the software in order to provide more accurate results. In that way, Voller's scheme can be easily extended to deal with non linear behavior in the phase diagram.

Considering the assumptions previously presented, the mixture equations for multicomponent solidification are the following:

Energy

$$\frac{\partial \rho c T}{\partial t} + \nabla \cdot (\rho_L c_L u T) = \nabla \cdot (k \nabla T) - \rho_S \Delta H \frac{\partial g}{\partial T} \quad [18]$$

Species

$$\frac{\partial \rho C}{\partial t} + \nabla \cdot (\rho_L u C_L) = 0 \qquad [19]$$

Mass

$$\frac{\partial \rho}{\partial t} + \nabla \cdot (\rho_L u) = 0 \qquad [20]$$

where g is the liquid volume fraction and u is the volume averaged fluid velocity defined as

$$u = g u_L \qquad [21]$$

Mixture density

$$\rho = \int_0^{1-g} \rho_S d\alpha + g\rho_L \qquad [22]$$

Mixture solute density

$$\rho C = \int_0^{1-g} \rho_S C_S d\alpha + g\rho_L C_L \qquad [23]$$

where ρc is the volumetric specific heat, taken as volume fraction weighted averages.

The boundary conditions are the following:

At $z = 0$ $\quad u = 0, k\dfrac{\partial T}{\partial z} = h_i(T_0 - T|_{z=0})$ and $\dfrac{\partial C_L}{\partial z} = 0$ [24]

At $z = Z_b$ $\quad T \rightarrow T_{pour}$ and $C \rightarrow C_0$ [25]

A. *Computational Algorithm*

Making use of the general scheme proposed by Voller,[18,32] this algorithm provides the solution of Eqs. [A5] through [A7], according to the following steps.

1. In problems with a eutectic reaction, temperature scales are translated such that $T_{eut} = 0$. This is then used as the reference temperature.
2. Initial iterate values ($n = 0$) are set to the old time-step values.
3. Equation [A6] is solved for the $[\rho C]$ nodal field.
4. Equation [A5] is solved for the auxiliary nodal temperature field, T^*. This step requires the evaluation, at each node, of the liquid fraction slope dg/dT.
5. From the T^* field, current nodal values for the liquid fraction are obtained from an appropriate form of Eq. [A4]; *i.e.,*

$$g_P^{n+1} = g_P^n + \text{SLOPE} \lfloor T_P^* - T_P^{equ} \rfloor \qquad [26]$$

where

$$T_P^{\text{equ}} = T_F - m_L[C_L]_P^n \qquad [27]$$

is the temperature obtained from the phase diagram and the term SLOPE in Eq. [26] is evaluated as

$$\text{SLOPE} = \begin{cases} \dfrac{dg}{dT}, & 0 < g_P^n < 1 \\[2mm] \dfrac{c_L}{\Delta H}, & g_P^n = 1 \text{ or } g_P^n = 0 \end{cases} \qquad [28]$$

In practice, Eq. [26] is applied at every node followed by an under-over-shoot correction to keep nodal liquid fractions in the interval between 0 and 1.

A critical step in the solution is the iterative evaluation of the liquid fraction-temperature slope, dg/dT. In this article, the same approximation used by Swaminathan and Voller[32] is adopted and seems to be very efficient, so

$$\frac{dg}{dT} = \begin{cases} \dfrac{g_P^n - g_P^{n-1}}{T_P^n - T_P^{n-1} + 10^{-6}}, & 0 < g_P^n < 1 \\[3mm] 0, & g_P^n = 1 \text{ or } g_P^n = 0 \end{cases} \qquad [29]$$

6. A microscale model is invoked to extract nodal values of liquid concentration C_L from the solute density field $[\rho C]$. The key variable in this calculation is the nodal liquid fraction calculated in the previous step. A detailed discussion has been previously presented by Voller,[18] in which the application of the back-diffusion model proposed by Wang and Beckermann[33] is suggested. The liquid concentration is given by

$$[C_L]_P = $$

$$\frac{[\rho C]_P - [\rho C]_P^{\text{old}} + \rho_L\, g_P^{\text{old}}\, C_L^{\text{old}} + \dfrac{\Delta t \gamma}{1 - g_P^{n+1}}[\rho C]_P}{\rho_L\, g_P^{n+1} + \rho_S\, k_0\left(g_P^{\text{old}} - g_P^{n+1}\right) + \dfrac{\Delta t \gamma}{1 - g_P^{n+1}}\left(\rho_S\, k_0\left(1 - g_P^{n+1}\right) + \rho_L\, g_P^{n+1}\right)}$$

$$[30]$$

where $\gamma = 0$ means the Scheil equation, and $\gamma \rightarrow \infty$ provides the lever rule;

7. In a binary eutectic system, if the liquid concentration calculated from the previous step exceeds the eutectic value, it is reset equal to this value.

8. The nodal temperature is calculated as

$$T_P^{n+1} = \begin{cases} T_F - m_L\,[C_L]_P^{n+1}, & 0 < g_P^n < 1 \\[2mm] T_P^*, & g_P^n = 1 \text{ or } g_P^n = 0 \end{cases} \qquad [31]$$

This establishes the nodal temperature to that of the equilibrium if node P is in the mushy zone or to the auxiliary value calculated in step 4 if P is not changing phase.

9. The last step in the iteration cycle is the updating of the mixture thermal constants such as conductivity, specific heat, and density; and the calculation of the velocity field using Eq. [20].

10. In the iteration cycle, steps 4 through 9 are repeated until convergence is reached; *i.e.*, in the implementation suggested by Voller, the convergence in time-step is reached when the maximum change in the nodal liquid fraction falls bellow 10^{-5}.

B. *Modifications*

The modifications that were introduced into the preceding numerical model discussed in Section A are needed for carrying out comparisons with the present experimental results, and are as follows:

1. a time variable global heat-transfer coefficient, which includes the metal/mold heat transfer coefficient; and
2. a Cartesian mesh adaptation to minimize effects of the nonlinearity boundary condition at the chill face, where interfacial unsteady heat transfer takes place.

1. *Global Heat-Transfer Coefficient*

For purposes of an accurate mathematical modeling, it is essential to establish trustworthy boundary conditions. The heat transfer that occurs at the metal/mold interface is one of these important conditions, which is a fundamental task during the early steps of the unsteady solidification process. The way heat flows through the ingot and the mold surface affects the evolution of solidification, and is of notable importance in characterizing the ingot cooling conditions, mainly for the majority of high heat diffusivity casting systems such as chill castings. When the metal comes into contact with the mold, at the metal/mold interface, the solid bodies are only in contact at isolated points and the actual area of contact is only a small fraction of the nominal area, as shown in Figure 2.

Part of the heat flow follows the paths of actual contact, but the remainder must pass through the gaseous and nongaseous interstitial media between the surface peaks. The interstices are limited in size, so that convection can be neglected. If temperature differences are not extreme, radiation does not play a significant role and most of the energy passes by conduction across the areas of actual physical contact.

The heat flow across a casting/massive mold interface, as shown by the schematic representation of Figure 2, can be characterized by a macroscopic average metal/mold interfacial heat-transfer coefficient (h_i), given by

$$h_i = \frac{q}{A(T_{IC} - T_{IM})} \qquad [32]$$

where q(W) is the global heat flux trough the interface; A is the area (m^2); and T_{IC} and T_{IM} are the surface ingot
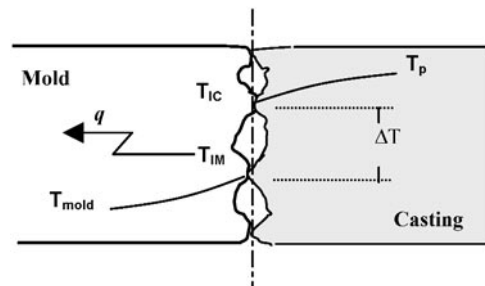

Fig. 2—Heat flux at the metal/mold interface.

temperature and the mold temperature (K), respectively. In water-cooled molds, the global heat flux is affected by a series of thermal resistances, as shown in Figure 3.

The interfacial resistance between the ingot surface and mold is generally the largest, and the global thermal resistance $1/h_g$ can be expressed in terms of

$$\frac{1}{h_g} = \frac{1}{h_W} + \frac{e}{k_M} + \frac{1}{h_i} \qquad [33]$$

where h_g is the global heat-transfer coefficient between the ingot surface and cooling fluid (W/m$^2 \cdot$ K), e is the bottom mold thickness (m), k_M is the mold thermal conductivity (W/m $\cdot$ K), and finally, h_W is the mold/cooling fluid heat-transfer coefficient (W/m$^2 \cdot$ K). The averaged heat flux from the ingot until the cooling water is given by

$$q = h_g (T_{IC} - T_O) \qquad [34]$$

where T_O is the temperature of water (Kelvin).
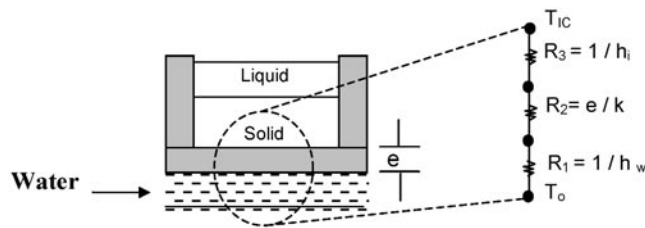
Fig. 3—Metal/coolant thermal resistances in a water-cooled metal/mold system.

A more detailed description and evaluation of transient metal/mold interface heat-transfer coefficients for Al-Cu and Sn-Pb systems can be found in an article by Santos et al.[34]

2. System Mesh Adaptation

The mesh system that uses a constant spatial interval dz throughout the ingot is very practical and common; nevertheless, it loses efficiency when a nonlinear time-dependent heat-transfer coefficient is introduced in the ordinary differential equation system, due to changes in the boundary $z = 0$. In order to avoid such a problem, the number of nodes N should be significantly increased so as to minimize the boundary effects. It is common knowledge that when the number of nodes is increased, more CPU time is required. Then, we have assumed changes in the space step size, according to the schematic representation shown in Figures 4(a) and (b) for discretization and shown in Figures 5(a) and (b) for discretization consequences in the temperature and concentration profiles. It can be seen that changes in temperature and concentration profiles are not so significant, but savings in computational time and computer storage requirements are substantial.

IV. EXPERIMENTAL PROCEDURE

The casting assembly used in solidification experiments has been detailed in previous articles[35–36] and is shown in Figure 6. The heat was extracted only through a water-cooled bottom, promoting upward directional solidification. A stainless steel mold was used having an internal diameter
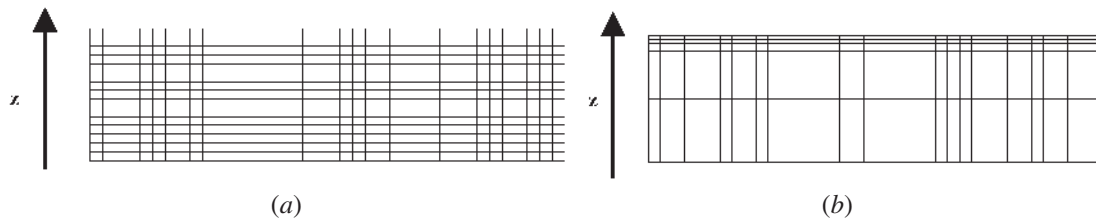

Fig. 4—(a) Constant mesh distribution and (b) variable mesh distribution along ingot.
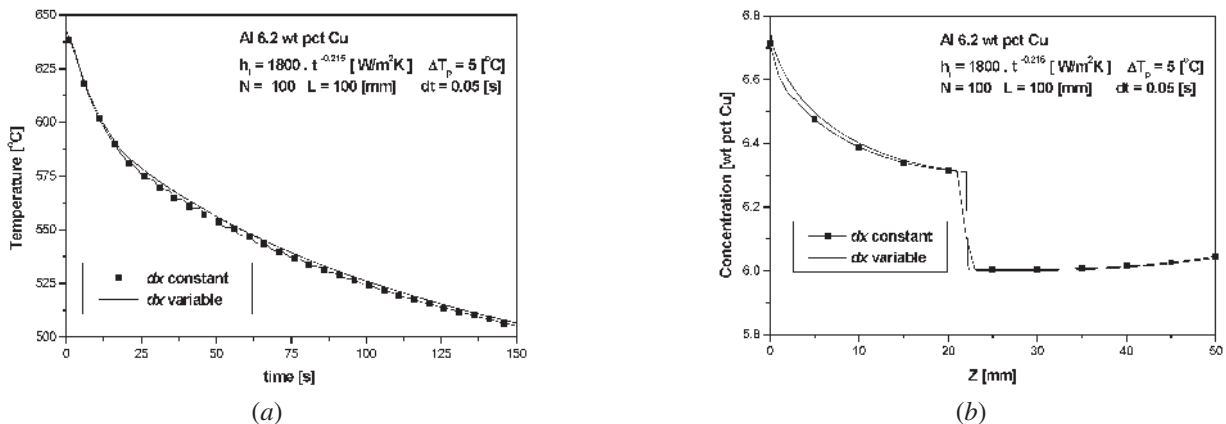

Fig. 5—(a) Comparison between thermal profiles in metal at 5 mm from the chill for constant and variable space grid and (b) concentration profiles for constant and variable space grid.
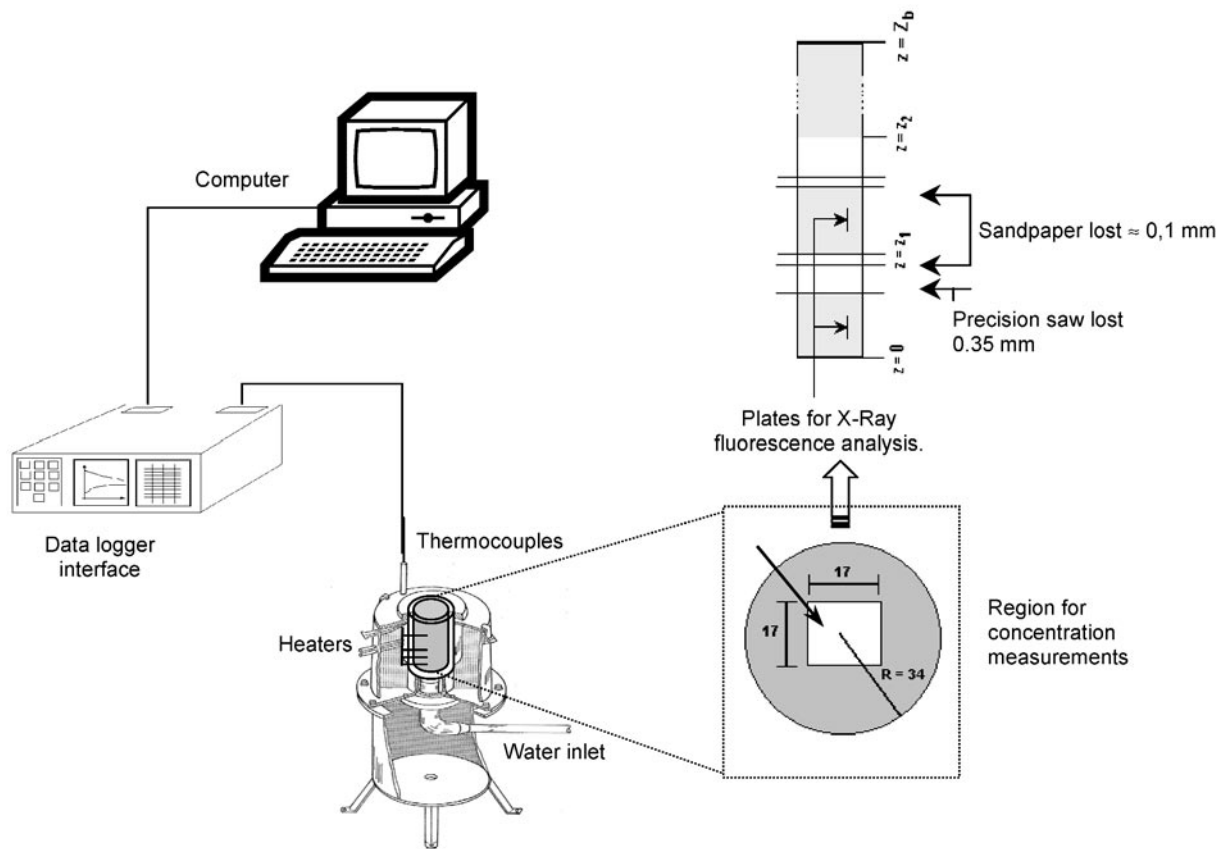
Fig. 6—Experimental apparatus and schematic representation of the samples used in the concentration analyses.

of 50 mm, height 110 mm, and wall thickness of 5 mm. The inner vertical surface was covered with a layer of insulating alumina to minimize radial heat losses, and a top cover made of an insulating material was used to reduce heat losses from the metal/air surface. The bottom part of the mold was closed with a thin (3 mm) carbon steel sheet with a roughness of about 35 μm. (In such a case, the error by ignoring the heat capacity of the bottom steel sheet mold, when applying Eq. [33] to determine h_g, is negligible.) The alloys were melted *in situ* and the lateral electric heaters had their power controlled in order to permit a desired superheat to be achieved. To begin solidification, the electric heaters were disconnected and at the same time the water flow was initiated.

Experiments were performed with Al 4.5 wt pct Cu, Al 6.2 wt pct Cu, and Al 8.1 wt pct Cu. To analyze the influence of melt superheat on the inverse segregation profiles, values about 20 °C, 60 °C, and 110 °C above the liquidus temperature were used during experiments with Al 6.2 wt pct Cu alloy. The thermophysical properties of these alloys are based on values reported in a previous article[34] and on the Thermo-Calc software, and are summarized in Table I.

Continuous temperature measurements in the casting were monitored during solidification *via* the output of a bank of fine type-*K* thermocouples sheathed in 1.6-mm o.d. stainless steel tubes, and positioned at 6, 11, 16, 29, and 46 mm from the heat-extracting surface at the bottom of the crucible. All of the thermocouples were connected by coaxial cables to a data logger interfaced with a computer, and the temperature data were acquired automatically.

The ingot was sectioned longitudinally and the macrostructure examined. It was then sectioned into transverse slices and a square central part was then cut by the use of a precision saw (BUEHLER ISOMET 4000* with

*BUEHLER ISOMET 4000 is a trademark of Buehler Ltd., Dusseldorf, Germany.

a 0.3-mm-thick diamond disk) into pieces of approximately 1.0 mm until 30 mm far from the chill, as shown in detail in Figure 6. The segregation samples were then underwent a RIGAKU Rix 3100 X-ray fluorescence spectrometer**

**Rigaku Rix 3100 X-ray is a trademark of Rigaku Corporation, Tokyo, Japan.

to estimate its average concentration through an area of 100 mm^2 probe. In some samples a wavelength dispersive spectrometry (WDS) analyses has also been performed in order to confirm the results obtained with the X-ray technique.

V. RESULTS AND DISCUSSION

The temperature files containing the experimentally monitored temperatures were used coupled with the numerical solidification program to determine the transient global metal/mold heat-transfer coefficient, h_g, as described in a previous article.[34] Figure 7 shows the temperature data collected in metal during the course of upward solidification

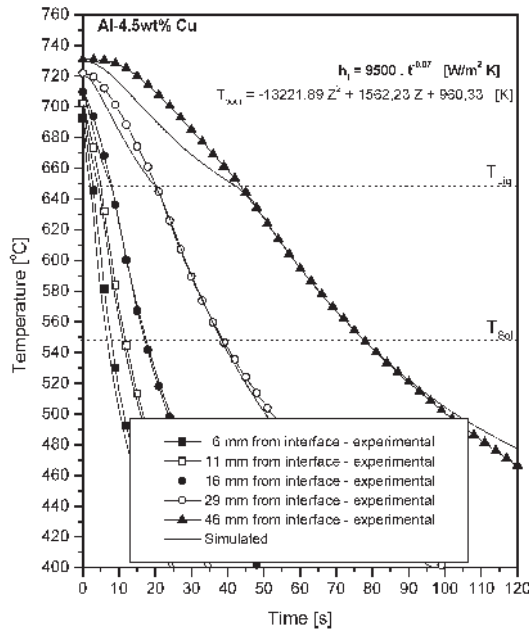of Al4.5 wt pct Cu, Al6.2 wt pct Cu, and Al8.1 wt pct Cu alloys in the vertical water-cooled mold.

The experimental thermal responses were compared with the predictions furnished by the numerical solidification model, and the best theoretical-experimental fit for each experiment has provided the appropriate transient h_g profile shown in Figure 8.

It can be seen in Figure 8 that the h_g profiles concerning the Al6.2 wt pct Cu alloy experiments decrease with increasing

Table I. Thermophysical Properties of Al-Cu Alloys Used in the Experimental Analysis[34]

| Properties	Units	Al 4.5 Wt Pct Cu	Al 6.2 Wt Pct Cu	Al 8.1 Wt Pct Cu
Thermal conductivity	k_S (W/m · K)	193	191	188
	k_L	89	88	86
	k_{SL}	141	139	137
Specific heat	C_S (J/kg · K)	1092	1089	1087
	C_L	1059	1049	1038
	C_{SL}	4995	5013	5205
Density	ρ_S (kg/m^3)	2654	2698	2748
	ρ_L	2488	2532	2582
	ρ_{SL}	2571	2615	2665
Thermal diffusivity	α_S (m^2/s)	6.66×10^{-5}	6.49×10^{-5}	6.30×10^{-5}
	α_L	3.38×10^{-5}	3.31×10^{-5}	3.24×10^{-5}
	α_{SL}	1.10×10^{-5}	1.06×10^{-5}	9.91×10^{-6}
Latent heat of fusion	ΔH (J/kg)	381,773	380554	379192
Fusion temperature	T_F (°C)	660	660	660
Solidus temperature	T_{Sol} (°C)	548	548	548
Liquidus temperature	T_{Liq} (°C)	648	644	639
Initial melt temperature	T_{pour} (°C)	712	664/707/757	654
ΔT_{pour}—melt superheat	(°C)	64	20/63/113	15
Solidification constants	ϕ_1	0.591	0.620/0.594/0.568	0.626
	ϕ_2	1.959	2.263/1.985/1.815	2.351
$(\alpha_S/\alpha_M)^{1/2}$	N	2.45	2.42	2.38
$(\alpha_S/\alpha_{SL})^{1/2}$	n	2.43	2.47	2.52
$(\alpha_{SL}/\alpha_L)^{1/2}$	m	0.58	0.57	0.55
$(k_S C_S \rho_S/k_M C_M \rho_M)^{1/2}$	M	0	0	0
Liquid-solid surface energy	σ_{SL} (J/m^2)	169×10^{-3}	169×10^{-3}	169×10^{-3}
Solute diffusivity	D_L (m^2/s)	3.5×10^{-9}	3.5×10^{-9}	3.5×10^{-9}
Solute composition	C_o (wt pct)	0.045	0.062	0.081
Liquidus slope	m_L (°C/wt pct)	-3.2	-3.2	-3.2
Partition coefficient	k_0	0.11	0.11	0.11
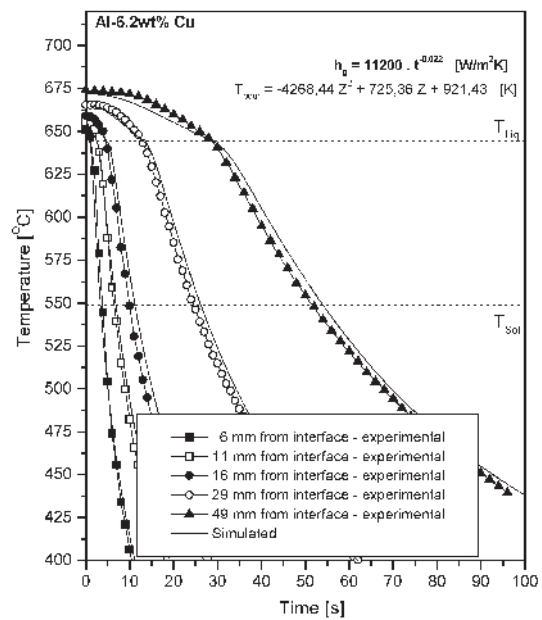
Fig. 7—Experimental thermal responses of thermocouples at five locations in casting from the metal/mold interface for (*a*) Al 4.5 wt pct Cu, (*b*) through (*d*) Al 6.2 wt pct Cu, and (*e*) Al 8.1 wt pct Cu compared with numerical simulations in order to determine h_g. (T_{pour} = initial variable melt temperature.)
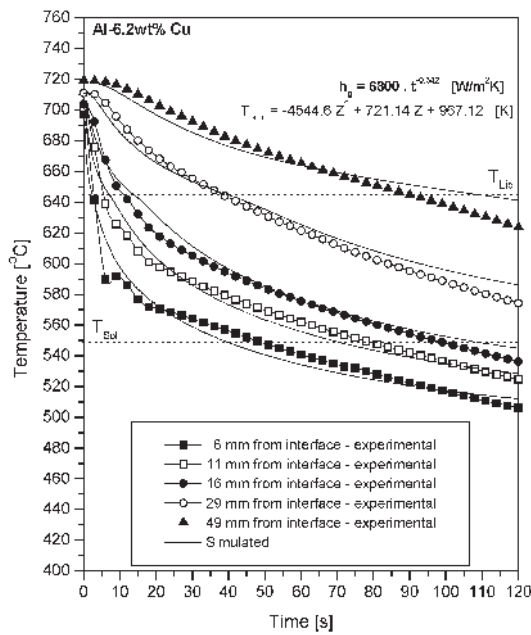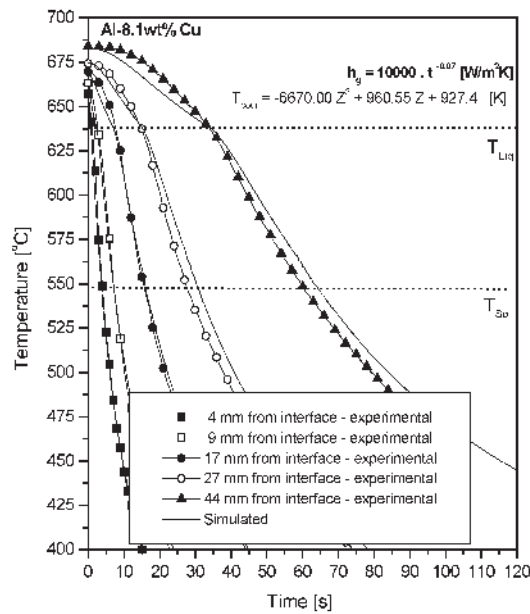
(c)
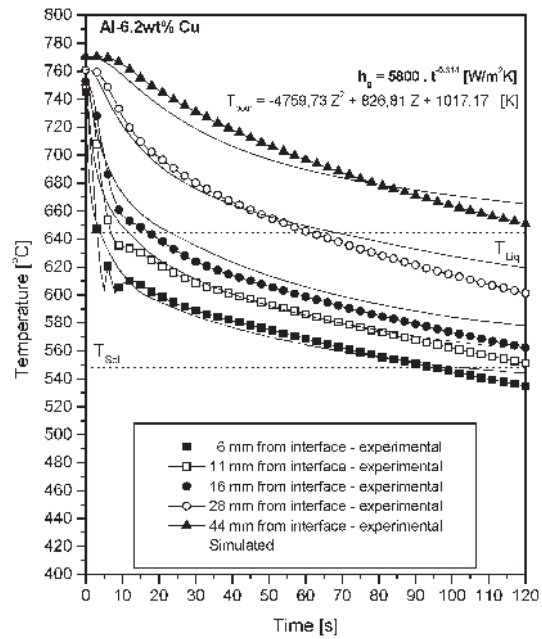
(d)

(e)

Fig. 7—(Continued). Experimental thermal responses of thermocouples at five locations in casting from the metal/mold interface for (a) Al 4.5 wt pct Cu, (b) through (d) Al 6.2 wt pct Cu, and (e) Al 8.1 wt pct Cu compared with numerical simulations in order to determine h_g. (T_{pour} = initial variable melt temperature.)

initial melt superheats, a tendency that is typical of the vertical upward unidirectional solidification, as observed and discussed in a recent article.[35] The transient h_g profiles were used in both the numerical and the analytical approaches in order to permit the necessary solidification parameters to be calculated. Figure 9 presents a comparison between experimental and analytical velocities of liquidus, V_L, and solidus, V_S, isotherms as a function of position, along the solidification experiments with Al6.2 wt pct Cu alloys. A fair to good agreement can be observed for the three different melt superheats experimentally examined. These variables are fundamental for

analytical calculations of inverse segregation profiles, as shown by Equations [13] and [14].

As the Al-Cu castings start to solidify from the bottom, and the rejected solute has a higher density than the melt, neither temperature nor solutal gradients will induce natural convection in the casting and the only possible driving force for fluid flow is solidification contraction. The experimental inverse solute distributions after the casting is completely solidified are shown in Figure 10 for Al4.5, 6.2, and 8.1 wt pct Cu alloys, respectively. A typical directionally solidified macrostructure observed on the Al-Cu ingots is also shown

in Figure 10(a). The inverse solute profile has occurred in the columnar zone in any case experimentally examined.

The concentration profile concerning the experiment with the Al 4.5 wt pct Cu alloy as determined by the X-ray analyses has been checked by a comparison with the results obta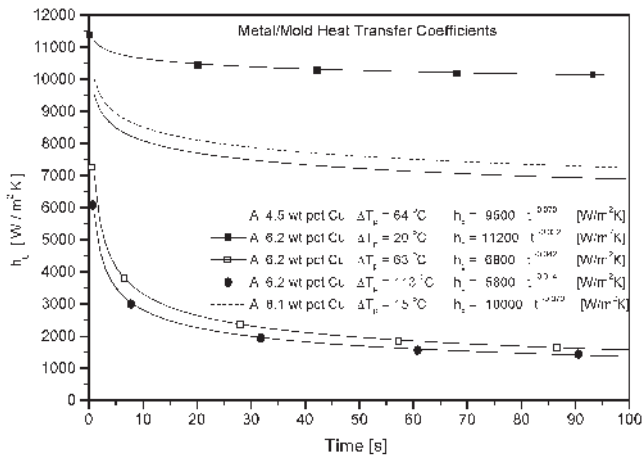ined by using a WDS technique. It can be observed in Figure 10(a) that the results from both techniques are very similar. The experimental inverse segregation profiles are compared in Figure 10 with calculated analytical and numerical theoretical results. It can be seen that the numerical predictions are in good agreement with the experimental results in any case examined. The predicted analytical segregation, despite its simplicity, also compares favorably with the experimental scatter except for the higher melt superheat used in experiments (and subsequent lower h_g profile: Al 6.2 wt pct Cu/ΔT_p = 113 °C) with the analytical model predicting a less severe inverse segregation close to the chill face than the experimental composition, as shown in Figure 10(d). The influence of the initial melt superheat on inverse segregation is associated with the resulting h_g profiles. A higher heat-transfer coefficient, which occurs for lower melt superheat, increases the cooling rate and decreases the size of the mushy zone. As a consequence, less solute can be carried by the fluid flow decreasing the severity of inverse segregation. That can be seen in Figure 10(b) by comparing the different experimental segregation profiles obtained for the Al 6.2 wt pct Cu alloy.

The numerical model permits inverse macrosegregation profile to be determined as a function of solidification processing variables. It can be used to gain insight into the foundry process, by preprogramming solidification in terms of some particular level of macrosegregation profile.

Fig. 8—Metal/coolant heat-transfer coefficient (h_g) as a function of time.
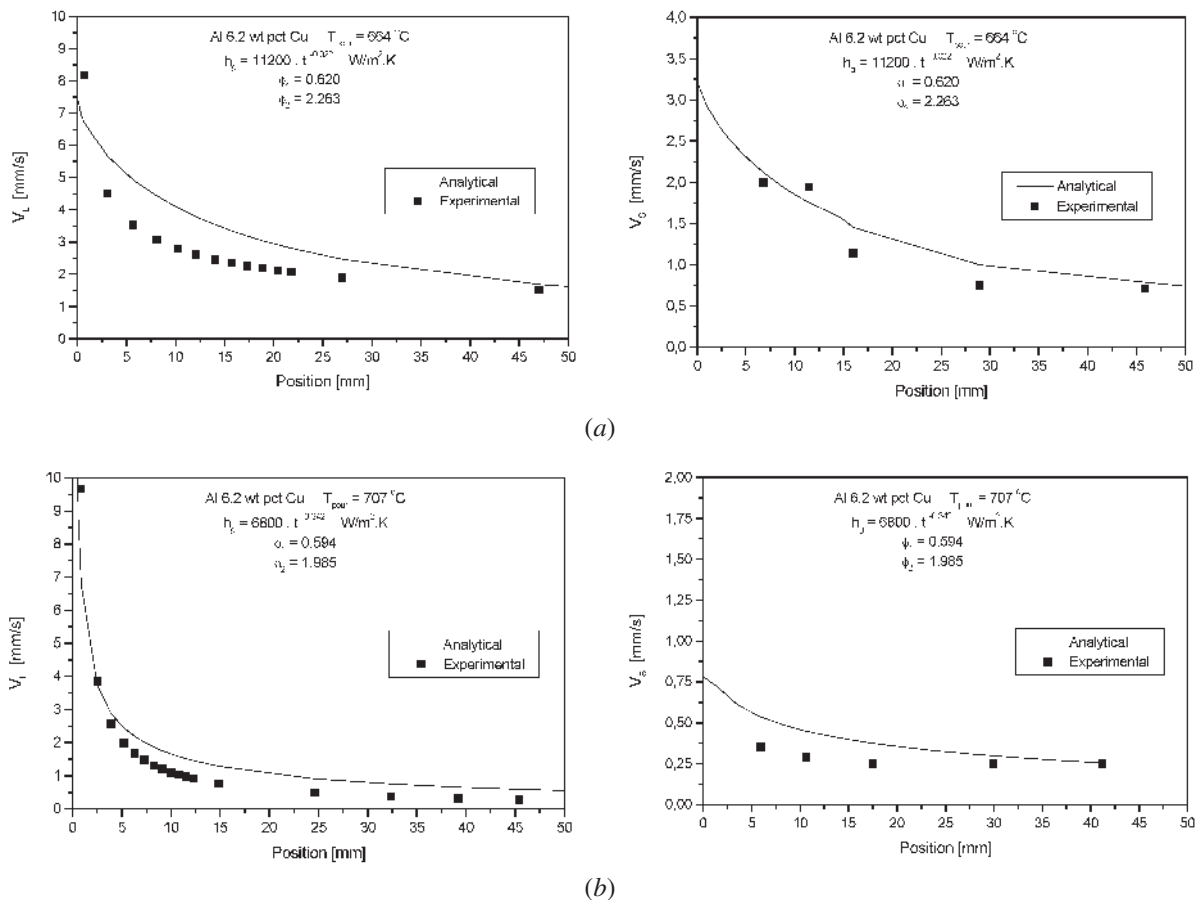

(a)

(b)

Fig. 9—Experimental and analytical velocities of liquidus and solidus isotherms as a function of position for Al 6.2 wt pct Cu alloy: melt superheats (a) 20 °C, (b) 63 °C, and (c) 113 °C.
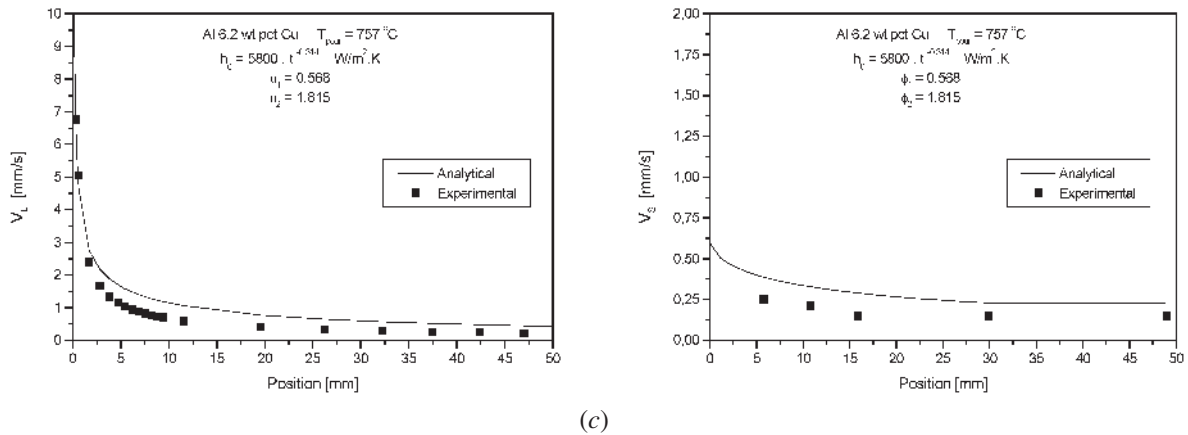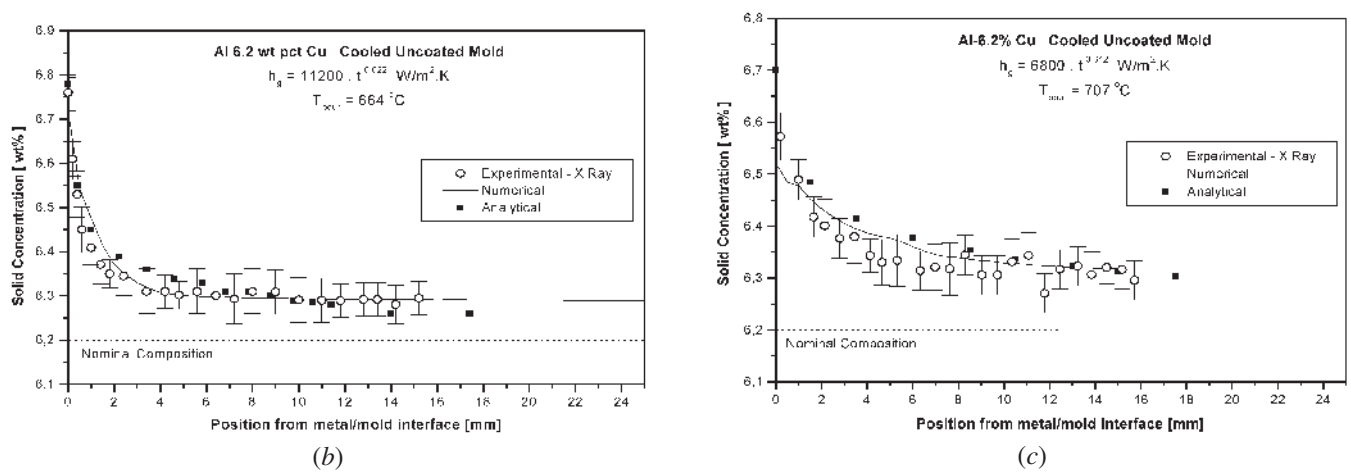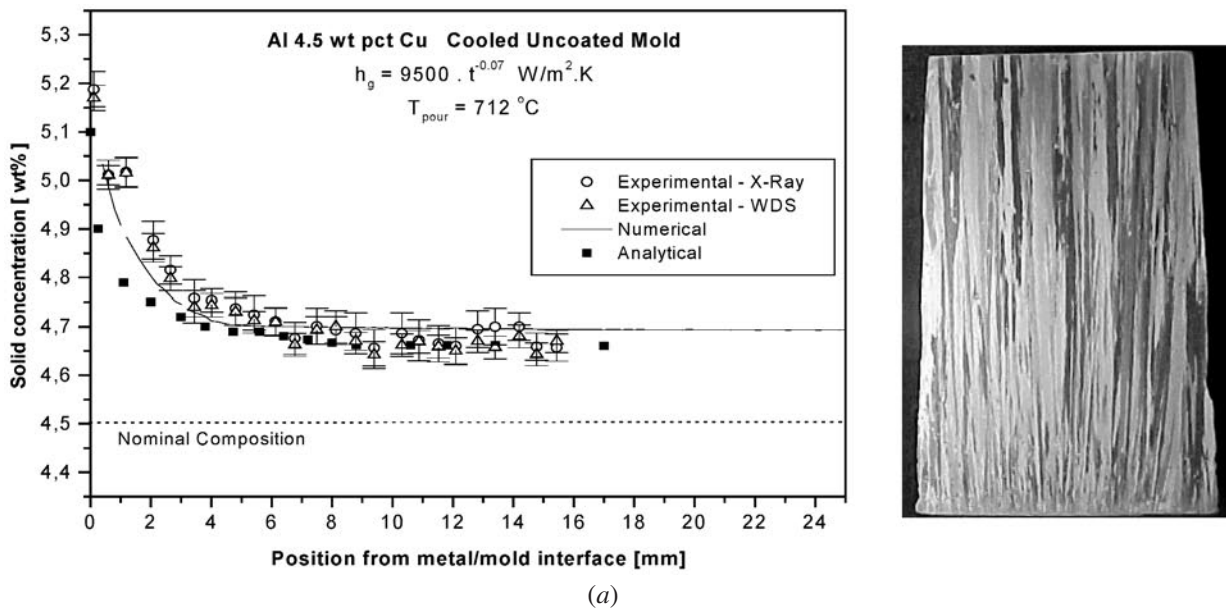
(c)

Fig. 9—(Continued). Experimental and analytical velocities of liquidus and solidus isotherms as a function of position for Al 6.2 wt pct Cu alloy: melt superheats (*a*) 20 °C, (*b*) 63 °C, and (*c*) 113 °C.

(a)

(b)

(c)

Fig. 10—Comparison between experimental and calculated inverse macrosegregation profiles for (*a*) Al 4.5 wt pct Cu, (*b*) through (*d*) Al 6.2 wt pct Cu, and (*e*) Al 8.1 wt pct Cu.
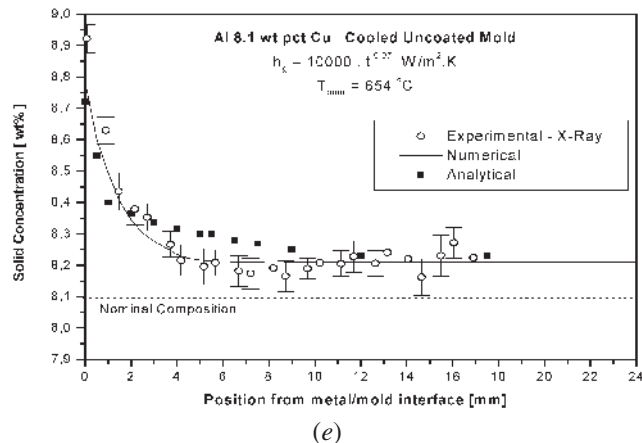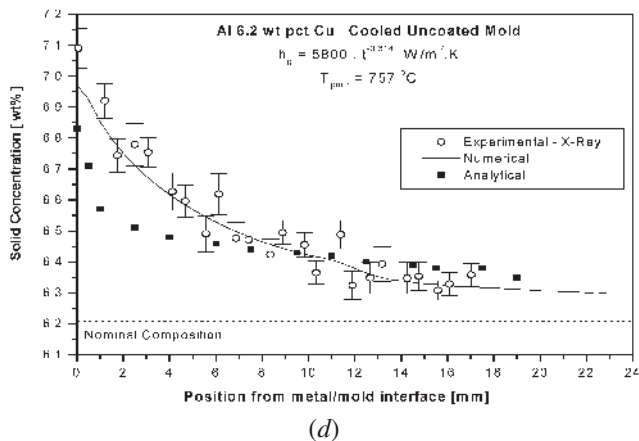
(d)

(e)

Fig. 10—(Continued). Comparison between experimental and calculated inverse macrosegregation profiles for (a) Al 4.5 wt pct Cu, (b) through (d) Al 6.2 wt pct Cu, and (e) Al 8.1 wt pct Cu.
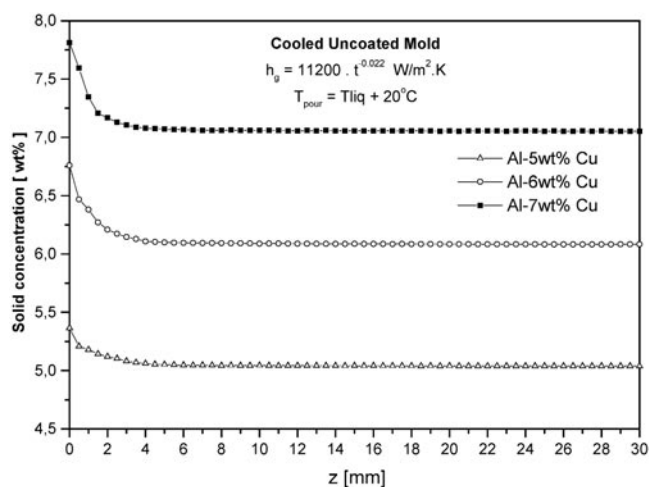

Fig. 11—Inverse macrosegregation profiles simulated for 30-mm-long unidirectional Al 5 wt pct Cu, 6 wt pct, and 7 wt pct Cu castings: $h_g = 11{,}200 \cdot t^{-0.022}$ W/m$^2 \cdot$ K.

Figure 11 illustrates the influence of alloy solute content concerning the simulation of 30-mm-long castings of Al 5, 6, and 7 wt Cu alloys solidified against a cooled mold with a same transient heat-transfer coefficient profile, $h_g = 11{,}200 \cdot t^{-0.022}$ W/m$^2 \cdot$ K. It is seen that in the region adjacent to the chill face, the inverse segregation drops rapidly with distance from the face. The initial slope of the curves (and hence the rate of decrease) is a function of the Cu content of the alloy, decreasing with increasing concentrations.

VI. SUMMARY

The following major conclusions are derived from the present study.

1. The numerical predictions are in good agreement with the inverse segregation experimental results in any case examined.

2. The predicted analytical segregation, despite its simplicity, also compares favorably with the experimental scatter except for the higher melt superheat used in experiments, $\Delta T_{pour} = 113$ °C, with the analytical model predicting a less severe inverse segregation close to the chill face than the experimental composition.

3. The analytical approach combines the advantage of generality and relative simplicity and can be easily manipulated to investigate the influence of solidification operational parameters on the final inverse solute distribution. It permits a complete analytical determination of the positional variation of segregation as a function of solidification thermal parameters such as thermal gradients, cooling rates, solid/mush, and mush/liquid interfaces velocities. It also permits the inverse segregation profiles to be directly correlated with solidification processing variables, *i.e.,* transient metal/mold heat-transfer coefficients, melt superheat and alloy, and mold thermophysical characteristics. On the other hand, the numerical model is more accurate, and can be used to encompass situations of two-dimension heat flow conditions, solidification of multicomponent alloys, and, with the argumentation of a momentum balance, is able to take into account the effects of thermal and solutal buoyancy.

4. The influence of the initial melt superheat on inverse segregation is associated with the resulting h_g profiles. A higher heat-transfer coefficient, which occurs for lower melt superheat, increases the cooling rate and decreases the size of the mushy zone. As a consequence, less solute can be carried by the fluid flow decreasing the severity of inverse segregation. The initial slope of the segregation profiles is a function of Cu content of the alloy decreasing with increasing concentrations.

APPENDIX A

Solution Scheme

Figure A1 shows a schematic representation of the solution scheme used for the development of the numerical model.

A fully time-implicit integration provides

$$a_P T_P^{n+1} = a_P^{old} T_P^{old} + a_S T_S^{n+1} + a_N T_N^{n+1} -$$

$$\rho_s \Delta H (g_P^{old} - g_P^{n+1}) \qquad [A1]$$

$$a_S = k_S \frac{\Delta t}{(\Delta z)^2}; \ a_N = k_N \frac{\Delta t}{(\Delta z)^2} - \frac{\Delta t}{\Delta z} \rho_L c_N u_n \qquad [A2]$$

$$a_P = k_S \frac{\Delta t}{(\Delta z)^2} + k_N \frac{\Delta t}{(\Delta z)^2} + \rho_L c_P - \frac{\Delta t}{\Delta z} \rho_L c_P u_S + a_P^{old};$$

$$a_P^{old} = \rho_L^{old} c_P^{old} \qquad [A3]$$

$$g_P^{n+1} = g_P^n + \frac{dg}{dT} [T_P^{n+1} - T_P^n] \qquad [A4]$$

Substitution of Eq. [A4] into Eq. [A1] results in the iterative equation

$$\left[a_P + \rho_S \Delta H \frac{dg}{dT} \right] T_P^* = a_P^{old} T_P^{old} + a_S T_S^* + a_N T_N^*$$

$$+ \rho_S \Delta H \frac{dg}{dT} T_P^n - \rho_S \Delta H (g_P^{old} - g_P^n)$$

$$[A5]$$

The solute conservation, Eq. [19], is discretized by the use of a fully explicit time integration scheme, and gives

$$[\rho C]_P = [\rho C]_P^{old} + \frac{\Delta z}{\Delta t} [\rho_L u_S [C_L]_P^{old} - \rho_L u_n [C_L]_N^{old}] \quad [A6]$$

The mass conservation, Eq. [20], is discretized as

$$u_N = u_S + \frac{\Delta z}{\Delta t} \left[\frac{\rho_P^{old} - \rho_P}{\rho_L} \right] \qquad [A7]$$

where values on the right-hand side are all determined with $(r + 1)th$ iterate values.

Considering the initial problem, applying a fixed chill temperature regarding Eqs. [26] through [28], we have

$$b_i = \rho^{old} c_P^{old} T_i^{old} + \rho_S \Delta H \left(g_P^{old} - g_P + \frac{dg}{dT} T_P^n \right) \quad [A8]$$
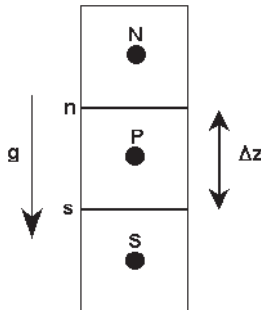

Fig. A1—Arrangement of control volumes.

Corrections for fluid flow:

$$a_P = a_P - \rho_L c_P u_P \frac{dt}{dz} \qquad [A9]$$

$$a_N = a_N - \rho_L c_P u_N \frac{dt}{dz} \qquad [A10]$$

Initial and boundary conditions:

$$b_2 = b_2 + a_{S(2)} T_L \qquad [A11]$$

$$b_{N-1} = b_{N-1} + a_{S(N-1)} T_N \qquad [A12]$$

REFERENCES

1. M.C. Flemings: *Solidification Processing,* McGraw-Hill, New York, NY, 1974, pp. 214-58.
2. M.C. Flemings: *Iron Steel Inst. Jpn. Int.,* 2000, vol. 40 (9), pp. 833-41.
3. S. Minakawa, I.V. Samarasekera, and F. Weinberg: *Metall. Trans. B,* 1985, vol. 16B, pp. 595-604.
4. E. Haug, A. Mo, and H.J. Thevik: *Int. J. Heat Mass Transfer,* 1995, vol. 38, pp. 1553-63.
5. H.J. Thevik and A. Mo: *Int. J. Heat Mass Transfer,* 1997, vol. 40, pp. 2055-65.
6. E. Scheil: *Metallforschung,* 1947, vol. 2, pp. 69-75.
7. J.S. Kirkaldy and W.V. Youdelis: *Trans. TMS-AIME,* 1958, vol. 212 (12), pp. 833-40.
8. W.V. Youdelis and D.R. Colton: *Trans. TMS-AIME,* 1960, vol. 218 (8), pp. 628-31.
9. J.R. Cahoon and W.V. Youdelis: *Trans. TMS-AIME,* 1964, vol. 230 (12), pp. 1734-34.
10. B. Prabhakar and F. Weinberg: *Metall. Trans. B,* 1978, vol. 9B, pp. 150-51.
11. H. Kato and J.R. Cahoon: *Metall. Trans. A,* 1985, vol. 16A, pp. 579-87.
12. M.C. Flemings and G.E. Nereo: *Trans. TMS-AIME,* 1967, vol. 239 (9), pp. 1449-61.
13. M.C. Flemings, R. Mehrabian, and G.E. Nereo: *Trans. TMS-AIME,* 1968, vol. 242 (1), pp. 41-49.
14. M.C. Flemings and G.E. Nereo: *Trans. TMS-AIME,* 1968, vol. 242 (1), pp. 50-55
15. Q.Z. Diao and H.L. Tsai: *Metall. Trans. A,* 1993, vol. 24A, pp. 963-73.
16. J.H. Chen and H.L. Tsai: *Int. J. Heat Mass Transfer,* 1993, vol. 36, pp. 3069-75.
17. S. Chang and D.M. Stefanescu: *Acta Mater.,* 1996, vol. 44, pp. 2227-35.
18. V.R. Voller: *Can. Metall. Q.,* 1998, vol. 37, pp. 169-77.
19. V.R. Voller: *Int. J. Heat Mass Transfer,* 1997, vol. 40, pp. 2869-77.
20. J.D. Chung, J.S. Lee, M. Choi, and H. Yoo: *Int. J. Heat Mass Transfer,* 2001, vol. 44, pp. 2483-92.
21. A. Garcia and M. Prates: *Metall. Trans. B,* 1978, vol. 9B, pp. 449-57.
22. A. Garcia and M. Prates: *Metall. Trans. B,* 1979, vol. 10B, pp. 85-92.
23. J.M.V. Quaresma, C.A. Santos, and A. Garcia: *Metall. Mater. Trans. A,* 2000, vol. 31A, pp. 3167-78.
24. W.R. Osório and A. Garcia: *Mater. Sci. Eng. A,* 2002, vol. 325, pp. 104-12.
25. O.L. Rocha, C.A. Siqueira, and A. Garcia: *Metall. Mater. Trans. A,* 2003, vol. 34A, pp. 995-1006.
26. I.L. Ferreira, C.A. Siqueira, C.A. Santos, and A. Garcia: *Scripta Mater.,* 2003, vol. 49, pp. 39-44.
27. S.V. Patankar: *Numerical Heat Transfer and Fluid Flow,* Hemisphere, New York, NY, 1980.
28. V.R. Voller and S. Sundarraj: *Int. J. Heat Mass Transfer,* 1995, vol. 38, pp. 1009-18.
29. J. Ni and C. Beckermann: *Metall. Trans. A,* 1991, vol. 22A, pp. 349-61.
30. C.A. Siqueira, N. Cheung, and A. Garcia: *J. Alloys Compounds,* 2003, vol. 351, pp. 126-34.
31. B. Sundman and Q. Chen: *STT Foundation (Foundation of Computational Thermodynamics),* Stockholm, Sweden, 1995.
32. C.R. Swaminathan and V.R. Voller: *Int. J. Heat Mass Transfer,* 1997, vol. 40, pp. 2859-68.
33. C.Y. Wang and C. Beckermann: *Metall. Trans. A,* 1993, vol. 24A, pp. 2787-2802.
34. C.A. Santos, J.M.V. Quaresma, and A. Garcia: *J. Alloys Compounds,* 2001, vol. 319, pp. 174-86.
35. C.A. Siqueira, N. Cheung, and A. Garcia: *Metall. Mater. Trans. A,* 2002, vol. 33A, pp. 2107-18.
36. O.L. Rocha, C.A. Siqueira, and A. Garcia: *Mater. Sci. Eng. A,* 2003, vol. 347, pp. 59-69.